



OPEN ACCESS

EDITED BY

Stanislaw Mazur,
Polish Academy of Sciences, Poland

REVIEWED BY

Liang Qiu,
China University of Geosciences Beijing,
China
Lei Gong,
Northeast Petroleum University, China

*CORRESPONDENCE

Jiajun Chen,
✉ chenjj_hz@petrochina.com.cn

RECEIVED 08 July 2023

ACCEPTED 07 September 2023

PUBLISHED 20 September 2023

CITATION

Deng X, Chen J, Cao P, Zhang Y, Luo X, Chang S, Shen J, Du Y and Wang M (2023), Segmentation and lateral growth of intracratonic strike-slip faults in the northern Tarim Basin, NW China: influences on Ordovician fault-controlled carbonate reservoirs. *Front. Earth Sci.* 11:1255162. doi: 10.3389/feart.2023.1255162

COPYRIGHT

© 2023 Deng, Chen, Cao, Zhang, Luo, Chang, Shen, Du and Wang. This is an open-access article distributed under the terms of the [Creative Commons Attribution License \(CC BY\)](https://creativecommons.org/licenses/by/4.0/). The use, distribution or reproduction in other forums is permitted, provided the original author(s) and the copyright owner(s) are credited and that the original publication in this journal is cited, in accordance with accepted academic practice. No use, distribution or reproduction is permitted which does not comply with these terms.

Segmentation and lateral growth of intracratonic strike-slip faults in the northern Tarim Basin, NW China: influences on Ordovician fault-controlled carbonate reservoirs

Xingliang Deng¹, Jiajun Chen^{2*}, Peng Cao², Yintao Zhang¹, Xiao Luo¹, Shaoying Chang², Jinlong Shen², Yifan Du² and Mengxiu Wang²

¹Research Institute of Exploration and Development, PetroChina Tarim Oilfield Company, Korla, China,

²PetroChina Hangzhou Research Institute of Geology, Hangzhou, China

Intracratonic strike-slip faults have been recognized as a major factor controlling the formation of fracture-cave carbonate reservoirs in deep buried basins, yet which properties and how the strike-slip faults influence reservoir distribution and their connectivity are still ambiguous. This uncertainty significantly restricts hydrocarbon exploration and development, such as in the Fuman oilfield, northern Tarim Basin, NW China. Using a high-resolution 3D seismic reflection survey and borehole data, we investigated the geometry and kinematic evolution of the F₁₇ fault zone in the Fuman oilfield. This fault zone is characterized by a single fault zone, pop-up or pull-apart structures, right-stepping en echelon normal faults, and much smaller displacement (<30 m) normal fault arrays from bottom to top. The F₁₇ fault zone consists of four genetic segments, including the extensional strike-slip duplex, Riedel left-lateral shear, right-stepping horsetail splay, and horizontal slip segments in map view. In particular, the formation of the ~18 km Riedel shear zone is characterized by the growth and linkage of segmented shear faults (synthetic and secondary synthetic shears). We observed that the large-scale fault-controlled fracture-cave reservoirs are distributed in positions with wider fault zones, which are characterized by overlapping of neighboring secondary shear faults. Furthermore, the reservoir width examined in this study is natural logarithmic correlated (positively) to the fault zone width. The reservoirs linked by the same shear faults show better internal connectivity. The spatial coherence between fault geometry and reservoir features indicates that segmentation and lateral growth of intracratonic strike-slip faults controls the occurrence of fracture-cave reservoirs, which may provide support for reservoir prediction in the Fuman oilfield and other deeply buried fault-controlled carbonate reservoirs in general.

KEYWORDS

fault segmentation, intracratonic strike-slip fault, kinematic evolution, fault-controlled carbonate reservoir, Tarim Basin

1 Introduction

An intracratonic strike-slip fault is defined as a fault with mainly horizontal displacement in a cratonic (intraplate) setting (Mann, 2007). Generally, strike-slip faults are characterized by rapid changes in structural style along the strike and with depth (Sylvester, 1988; Dooley and Schreurs, 2012). In map view, a strike-slip fault may exhibit a complex spatial arrangement of different associated structures, including releasing bends, restraining bends, principal displacement zones, and horsetail splays (Pakiser, 1960; Clayton, 1966; Tchalenko, 1970; Woodcock and Fisher, 1986). In experimental studies, a specific arrangement of associated structures is identified as a recorder for indicating a corresponding growth and linkage pattern of a fault zone (Tchalenko, 1970; Woodcock and Fisher, 1986), helping to understand the formation mechanism of strike-slip faults. Recently, many studies have revealed the spatiotemporal coherence between intracratonic strike-faulting and carbonate reservoir distribution (fault-controlled fracture-cave reservoirs), pointing out that faults control the distribution of this type of reservoir (Han et al., 2017; 2018; 2020; Wang et al., 2017; Deng et al., 2018; 2019; Ning et al., 2018; Ma et al., 2019; Tian et al., 2021; Qiao et al., 2023). Remarkably, the fault-controlled fracture-cave reservoirs of the Fuman oilfield in the northern Tarim Basin, NW China, have established a 3 million t oil production base (as of 2022). Therefore, uncovering the nature and mechanics of strike-slip faults is essential not only for theoretical research but also for promoting the exploration and development of fault-controlled fracture-cave reservoirs.

The F₁₇ fault zone in the Fuman oilfield provides an extraordinary example to illustrate the geometry and kinematic evolution of intracratonic strike-slip faults. Previous studies have revealed that a long-distance strike-slip fault zone in the central Tarim Basin consists of multiple pull-apart, pop-up, and horizontal slip segments (Qi, 2020; Yun, 2021). The reservoir distribution varies with different fault zones and with different segments of the same fault zone. Furthermore, the opening status of faults is mainly controlled by the present stress field, influencing lateral reservoir connectivity. The larger the angle between the orientations of the principal stress and fault zone is, the better the reservoir connectivity (Qi, 2020). With this knowledge, the Fuman oilfield is full of commercial oil flow wells even at a depth of >8,000 m. However, with the production process, many boreholes confirm that the previous knowledge on segmentation, i.e., pull-apart, pop-up, and horizontal slip segments cannot meet the production requirements. For example, the previous segmentation does not predict the lateral connectivity of adjacent reservoirs. This contradiction seriously affects the evaluation of reservoir unit division, which is an important part of reserve calculation and development programming.

The previous segmentation principle of the intracratonic strike-slip fault zone is mainly based on the structural style in sectional view (Liu et al., 2020; Zhou et al., 2022), namely, geometric segmentation. A more reasonable segmentation principle should consider the lateral growth and linkage of strike-slip faults (e.g., Deng et al., 2019; Liu et al., 2023) and recognize oriented shear faults (fractures) in the shear zone; an example of a reasonable segmentation model is the Riedel shear model (Aydin and Page,

1984; Sylvester, 1988). This segmentation principle is consistent with our knowledge of the formation mechanism of strike-slip faults, which has been confirmed by Riedel clay experiments and several numerical modeling experiments (e.g., Asaoka et al., 2016). We suggest that determining the genetic segmentation of strike-slip faults may provide a more profound understanding of fault formation and a more reasonable explanation for reservoir distribution and connectivity.

To characterize the geometry and kinematic evolution of intracratonic strike-slip faults and to determine the specific relationship between fault segmentation and reservoir distribution, this study characterized the structural framework of the F₁₇ fault zone based on a high-resolution 3D seismic survey and quantities of borehole data. Following the growth mechanism of the strike-slip fault, we redivided the F₁₇ fault zone into four genetic segments. Each segment is composed of different structural elements (e.g., synthetic, antithetic, and secondary synthetic shears). With borehole calibration, we measured the width of the fault zone and reservoir width along the strike that directly reflects their lateral changes. The reservoir width examined in this study is natural logarithmic correlated (positively) to the fault zone width. Finally, we find that the overlapping position of adjacent shear faults is conducive to the formation of large-scale reservoirs. Different from the previous geometrical segmentation (pull-apart, pop-up, and horizontal slip segments), the genetic segmentation that considers the lateral growth of strike-slip faults explains why the interconnected reservoirs are mainly distributed along the same fault surface.

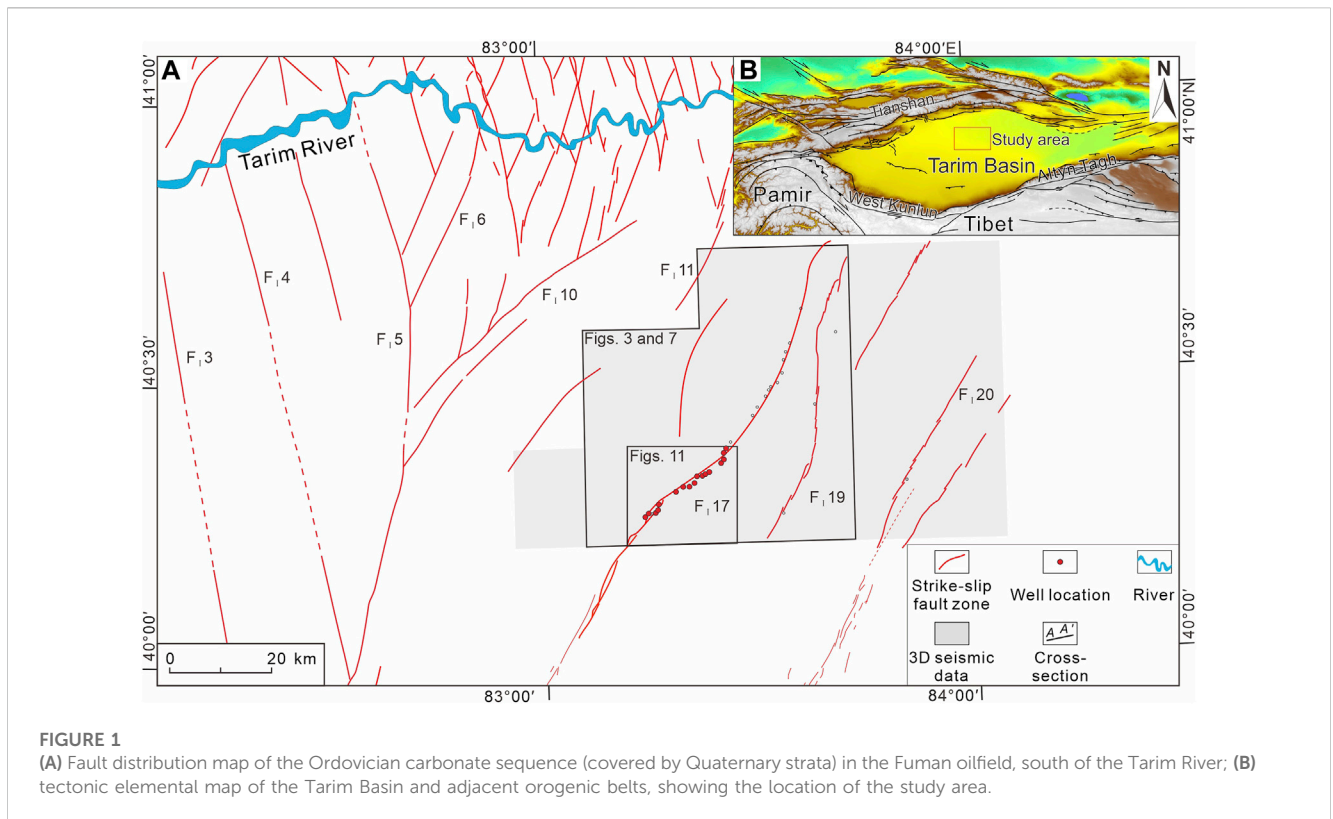
2 Geological setting

The F₁₇ fault zone is located in the central Tarim Basin (the northern margin of the Qinghai-Tibetan Plateau), which is surrounded by the Tianshan Mountains to the north, the West Kunlun Mountains to the southwest, and the Altyn Tagh Mountains to the southeast (Figure 1). This fault zone (concentrated in the Cambrian to Ordovician sequence) strikes northeast and has a length of ~72 km (within the 3D seismic survey).

2.1 Tectonic evolution

The Tarim Basin is a composite and superimposed sedimentary basin that formed on a cratonic basement (Jia, 1997; He et al., 2005). Multiple findings, such as differences in the composition of the basement (Yang et al., 2014), the presence of a W-E-oriented high magnetic anomaly zone (Yuan, 1996), and primary paleomagnetic results, suggest that the Tarim Craton was finally assembled in the Early Neoproterozoic (Zhao et al., 2021). The Neoproterozoic evolution of the basin can be divided into three stages: 1) the rifting stage (760–700 Ma); 2) the rifting to depression transitional stage (660–600 Ma); and 3) the post-rift depression evolution stage (580–540 Ma) (Shi et al., 2018).

From the Cambrian to Middle Ordovician, the Tarim Craton was subjected to an extensional tectonic setting, corresponding to the opening of the Proto-Tethys Ocean (He et al., 2005). Since the Late Ordovician, the southern margin of the Tarim Craton has transformed into a compressional setting, corresponding to the



closure of the Proto-Tethys Ocean (Matte et al., 1996; Jia, 1997; Zhang et al., 1999; Xu et al., 2006). This compressional setting caused the formation of the intracratonic strike-slip fault zone (in the Ordovician carbonate sequence) (Deng et al., 2018; Huang, 2019; Sun et al., 2021; Chen et al., 2022). *In situ* laser ablation inductively coupled plasma–mass spectrometry (LA–ICP–MS) U–Pb dating of the calcite cements in these fault zones indicates that the strike-slip fault (or possibly a certain strike-slip fault) initiated at ~460 Ma (Yang et al., 2021). There are three stages of key tectonic events for strike-slip faults during the Paleozoic: 1) end of the Middle Ordovician; 2) end of the Ordovician; and 3) end of the Middle Devonian (Huang, 2019). During the Late Devonian–Permian, the northern margin of the Tarim Craton experienced scissor-like, east-to-west closure of the South Tianshan Ocean and subsequent collision (Jia, 1997; Chen et al., 1999; Gao et al., 2009). The intracratonic strike-slip fault zone reactivated correspondingly in this stage (Huang, 2019). At the southern margin of the Tarim Craton, a passive margin was formed due to the opening of the Paleo-Tethys Ocean (Xu et al., 2006). From the Jurassic to the Eocene, a multiphase extensional setting occurred due to the evolution of the Neo-Tethys Ocean (He et al., 2005). During the Cenozoic, the far-field effect of the India–Eurasia collision influenced the whole basin (Sobel and Dumitru, 1997), while the F₁₇ fault zone was deeply buried.

2.2 Stratigraphy

The stratigraphic column in the Fuman oilfield contains sedimentary layers from the Nahua system (Neoproterozoic) to

the Quaternary, with a total thickness of ~11 km. The uppermost ~2,400 m of Cenozoic strata contains Quaternary, Neogene, and Paleogene strata, which are in unconformably contact with each other (Figure 2). These sequences are composed of conglomerates, sandstones, and mudstones. They exhibit multiple rhythms and generally coarsen upward. Mesozoic strata (approximately 1,400 m thick) are composed of Lower Cretaceous, Lower Jurassic, and Triassic strata. The Lower Cretaceous strata are characterized by fine-grained sandstones interbedded with mudstone. In particular, the lower part of this sequence has a high feldspar content while the upper part has a high lithic content. Unconformably overlain by the Lower Cretaceous strata, the Lower Jurassic strata only have a thickness of <150 m, and the lithology consists of sandstones interbedded with mudstones. The Triassic strata with a thickness of ~770 m consist of mudstones, silty mudstones, and lithic sandstones. At the bottom of this sequence, gravels and fine-grained lithic sandstones unconformably overlie the Paleozoic sequence.

The upper Paleozoic sequence consists of Permian igneous rocks and clastic rocks, Carboniferous marine clastic rocks interbedded with limestone, and Upper Devonian sandstone and siltstone (Figure 2). The thickness of this sequence is in the range of 1,300–1,400 m. The lower Paleozoic sequence is mainly characterized by lower Cambrian and upper Cambrian to Middle Ordovician carbonates, middle Cambrian gypsiferous rocks, Upper Ordovician mudstone, and Silurian clastic rocks. The Sinian (Ediacaran) strata consist of clastic rocks and dolomite in sequence. At the bottom of the sedimentary sequence, Nahua coarse clastic rocks are distributed sporadically in Neoproterozoic rifts. In general, the stratigraphic composition can be subdivided

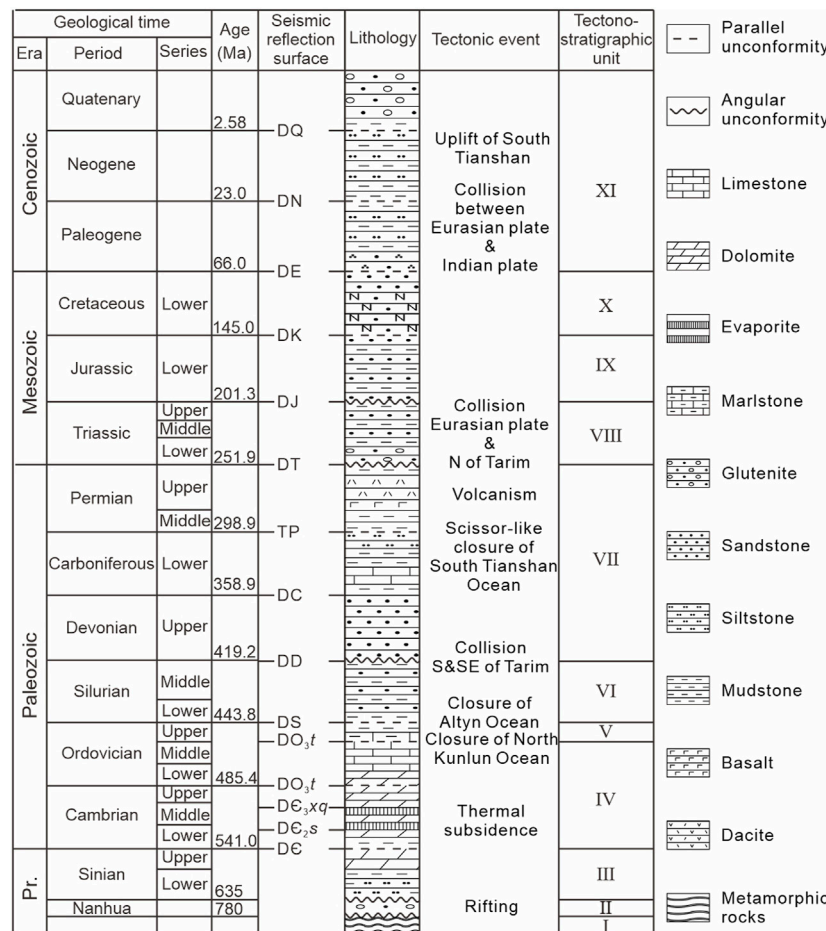


FIGURE 2 Stratigraphic column and tectonic stages of the Fuman oilfield, northern Tarim Basin (modified after [Chen et al., 2022](#)).

into 11 tectonostratigraphic units based on the regionally distributed unconformities.

2.3 Interwell connectivity

In recent well production, approximately thirty wells confirm that the reservoirs are widely distributed along the F₁₇ fault zone. Fault-enlarged caves, and fracture-enlarged pores in the fault zone are the main types of reservoir spaces. Similar to the features of strike-slip faults, the reservoir distribution also exhibits rapid changes in structural style along strike and with depth (e.g., [Deng et al., 2022](#)). As these wells have been successively put into production, a mass of dynamic data provides a comprehensive understanding of the interwell connectivity. On the other hand, the seismic inversion results based on a high-resolution seismic reflection survey also help us determine the reservoir connectivity. Combined with pressure changes, interwell interference analysis, changes in oil pressures and production, and seismic inversion of reservoirs, the Tarim Oilfield Company (CNPC) has confirmed four connected well groups in the southwest part of the 3D seismic survey area ([Figure 1](#)). These four connected well groups contain (I) ManS4, ManS4-H3, ManS4-H2, and ManS4-H1; (II) ManS2, ManS1, and

ManS1-H2; (III) ManS1-H1, ManS3-H8, ManS3-H7, and ManS3-H6; and (IV) ManS3 and ManS3-H2 ([Figure 3](#)). Subsequently, the reservoirs penetrated by these wells are supposedly connected and are thus classified into a unified reservoir unit.

3 Data and methods

This study utilized a high-resolution and prestack depth-migrated 3D seismic reflection survey from PetroChina Tarim Oilfield Company. The survey has a total areal extent of 4,700 km², record depth of 18 km, line spacing of 25 m (inline) * 12.5 m (crossline), and vertical resolution of ~65 m at the interval of interest ([Figure 1](#)). Seventeen boreholes, which contain conventional logs and original well reports, were used to constrain the age of mapped seismic horizons and lithologic variations within the stratigraphic units that they bound. Ten horizons were interpreted ([Figure 2](#)), including the base of the lower Cambrian (D_C), base of the middle Cambrian (D_{C2s}), base of the upper Cambrian (D_{C3xq}), base of the Middle Ordovician Yijianfang Formation (D_{O2y}), base of the Upper Ordovician Tumuxiuke Formation (D_{O3t}), base of the Silurian (DS), base of the Carboniferous (DC), base of the Permian (DP), base of the

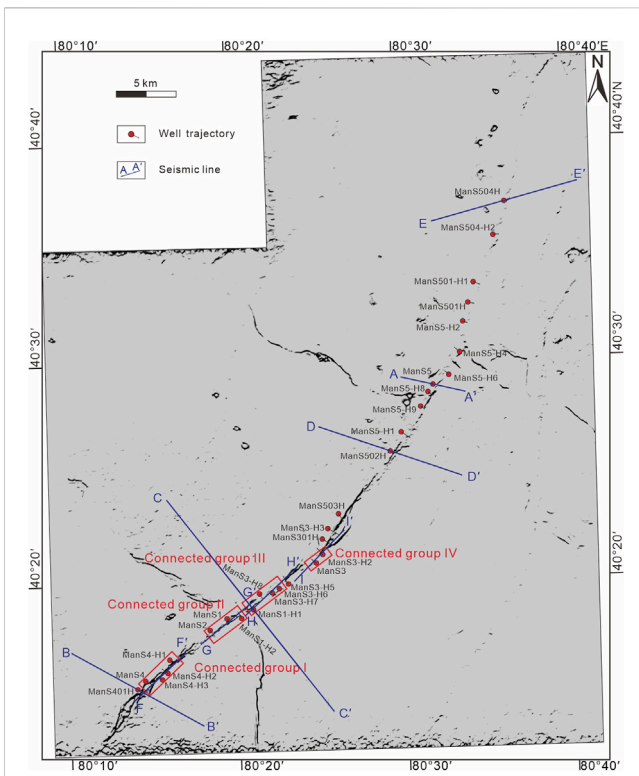


FIGURE 3
Coherency attribute signature (surface of the DO_{3t} , base of the Tumuxiuke Formation) showing the fault distribution of the F_{17} fault zone and four confirmed connected well groups.

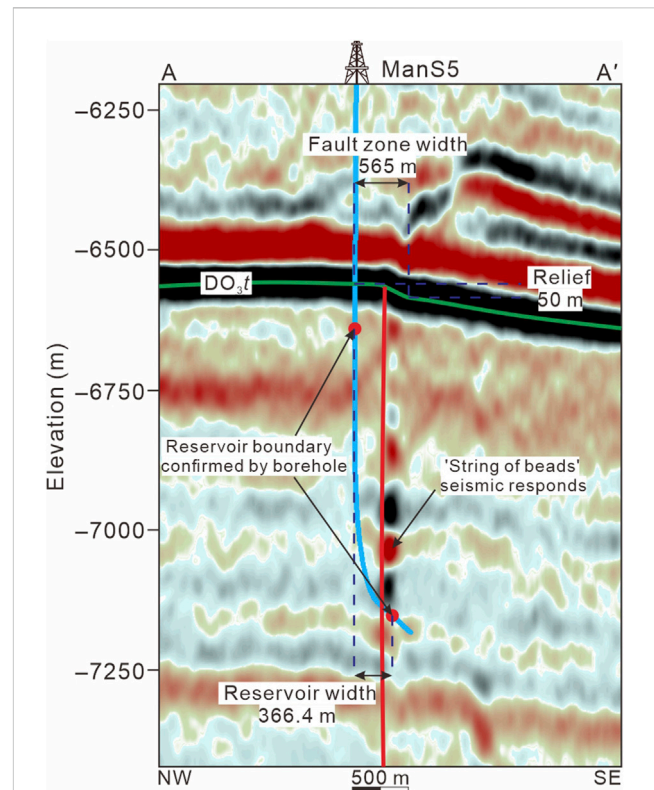


FIGURE 4
Practical example demonstrating the method to measure the fault zone width, reservoir width, and structural relief in seismic cross-section AA' (see Figure 3 for location). The green line indicates the base of the Tumuxiuke Formation. The fault zone penetrated by well ManS 5 has a width of ~565 m and a structural relief of ~50 m. The reservoir width measured from seismic reflection data that is validated by borehole data (well ManS 5) is ~366.4 m.

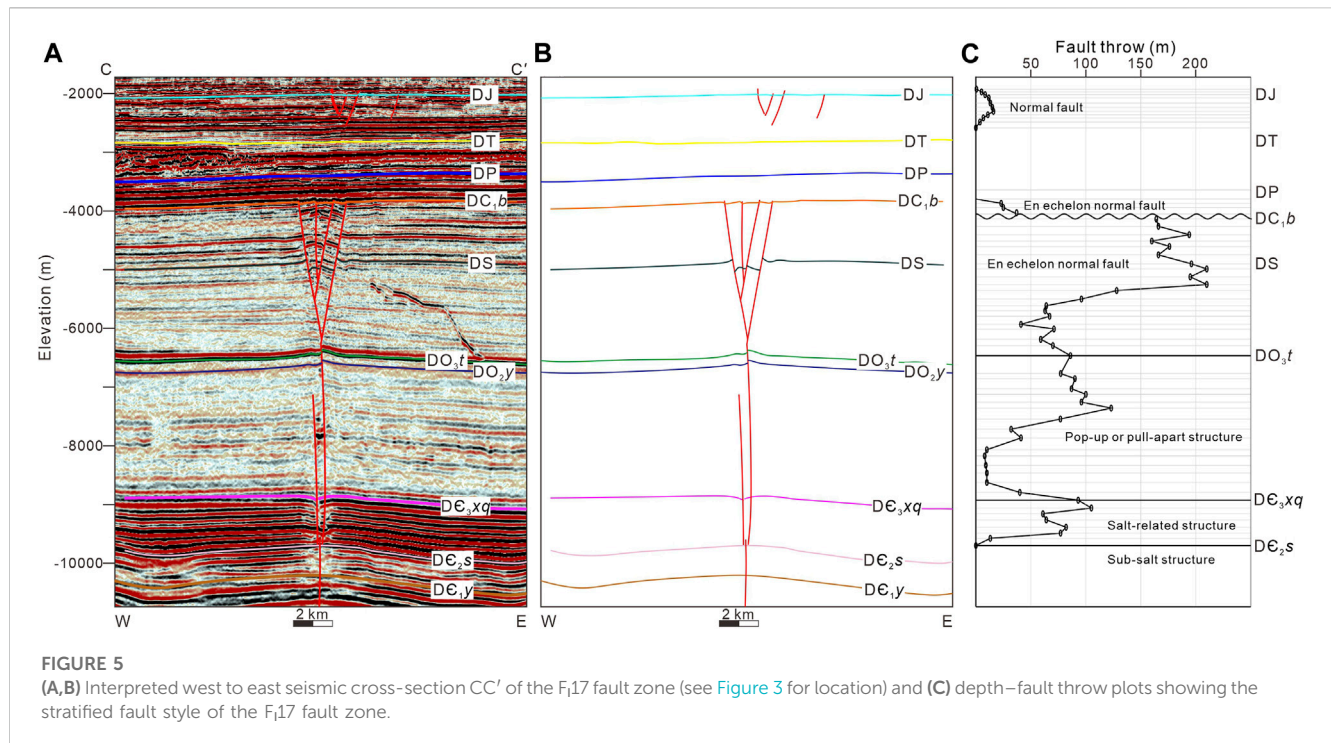
Triassic (DT), and base of the Jurassic (DJ). Two key seismic horizons were mapped across the study area (DO_{3t} and DS). For fault and reservoir identification, we interpret a fault when obvious faulting or discontinuity of seismic reflectors are exhibited in seismic cross-sections and coherence slices (Figures 3–6). Specifically, “string of beads” seismic responses are the integrated response of the top and bottom reflections as well as the faint multiples of carbonate reservoirs (Li et al., 2012).

Depth–throw plots were used to analyze the stratified style of faults and fault growth history. Generally, the depth–throw pattern of a single fault exhibits a normal distribution (e.g., Walsh and Watterson, 1988; Cartwright et al., 1996; Walsh et al., 2003; Whipp et al., 2017), namely, fault displacement decreases from core to tip, helping to identify different faults with depth. Along-strike variations in structural relief (including fold relief and fault throw) on the F_{17} fault zone, which provide information on its segmentation and structural styles, were constrained by measuring the reliefs between highest or lowest points in the fault zone and reference level (Figure 3). The fault zone width and reservoir width along strike were also measured. In particular, the fault zone width is defined as a deformation zone that is caused by faulting (Figure 4). In fault anatomy, a mature fault zone contains a fault core, damage zone (brittle), and drag zone (ductile) (Fossen, 2016). We measured the boundary points of the folded horizon (DO_{3t}) to represent the width of the fault zone (width of drag zones). Reservoirs are characterized by leakage of drilling fluid, evacuation, gas measurement display, and “string of beads” seismic responses.

These wells mostly drill perpendicular to the fault zone; thus, the width measured from the abovementioned information (validated) represents the reservoir width across the fault zone. Finally, a reservoir width–fault zone width plot is presented to determine the relationship between them.

4 Structural framework of the F_{17} fault zone

Similar to other intracratonic strike-slip fault zones in the Tarim Basin, the F_{17} fault zone shows rapid changes in structural styles along strike and with depth (Figure 3). In sectional view, a vertical single fault is present below the middle Cambrian salt layer (Figure 5). The throw of this fault is too small to measure in the seismic reflection survey. Instead, this subsalt structure is characterized by low-amplitude folds, with a structural relief of ~336 m. The suprasalt faults in the upper Cambrian to Middle Ordovician strata mainly form pop-up (positive flower), pull-apart (negative flower) or horizontal slip structures (Figures 5, 6A, B, D; Sun et al., 2021). The throw of this fault array increases upward (up to ~120 m). In the Upper Ordovician to Silurian sequence, a typical negative flower structure is recognized, composing a series of right-



stepping en echelon normal faults in map view (Figure 7B). The throw of this fault array is larger than the underlying throw and increases upward (up to ~200 m). A notable point is that the unconformity between the middle Silurian and lower Carboniferous is also faulted (Figure 5). The throw of this fault array in the Carboniferous strata decreases abruptly upward (~37 m). In the Triassic to Jurassic sequence, a series of normal faults above the F₁₇ fault zone is also recognized, with a throw of ~20 m.

In map view, the F₁₇ fault zone revealed by a 3D seismic reflection survey strikes NE40° in the southwest part (Figure 7A). The base of the Tumuxiuke Formation exhibits positive relief in the central area and negative relief at the two ends (Figure 7A). The base of the Silurian exhibits a series of right-stepping en echelon normal faults, with a strike range of NW20°–NE10°. In the northeastern part, this fault zone in the Middle Ordovician sequence is curved, striking NE35° to NE5° from south to North. The relief of the fault zone is much smaller than that in the southwest part. The structural map of the base of the Silurian shows that both the length and distribution range of right-stepping en echelon normal faults increase northeastward and that the strikes of these faults transform into N–S trends, forming classic horsetail splays (Sylvester, 1988).

In summary, the structural framework of the F₁₇ fault zone is characterized by multiple layers of fault arrays, including subsalt single faults, suprasalt push-up or pull-apart stepping faults, and en echelon normal faults from bottom to top (Sun et al., 2021; Chen et al., 2022). The F₁₇ fault zone shows both positive and negative relief, indicating a rapid change in the structural style along strike. The relief–distance plots show four parts from southwest to northeast, namely, 1) negative (<209 m), 2) positive (<186 m), 3) negative (<164 m), and 4) nonvertical relief parts (Figures 6, 7). This plot pattern indicates that the F₁₇ fault zone can be subdivided into four corresponding segments (Figure 7).

5 Segmentation of the F₁₇ fault zone

According to the different combinations of strike-slip fault elements, the F₁₇ fault zone can be segmented into the 1) extensional strike-slip duplex (Figure 6A); 2) Riedel left-lateral shear zone (Figure 6B); 3) right-stepping horsetail splay (Figure 6C), and 4) principal slip zone (Figure 6D) from southwest to northeast (Figure 7).

5.1 Extensional strike-slip duplex

In map view, the negative structural relief penetrated by wells ManS401H and ManS4 shows a typical extensional structure (Figures 7A, 8A). In sectional view, the rocks between two boundary faults (two independent principal displacement zones; PDZ1 and PDZ2) subside, forming a rhombic graben (Figure 6A). The graben has a length of ~4.0 km and a width of ~1.0 km (Figure 7). The maximum offset of the graben is up to 200 m (Figure 8B). Within the rhombic graben, a series of nearly North–South-striking normal faults are linked to the two northeast–southwest boundary faults, forming a classic negative flower structure. Left-stepping strike-slip faults with extensional settings indicate that the kinematic evolution of this fault segment underwent left-lateral slip, forming a typical extensional strike-slip duplex (Woodcock and Fischer, 1986). Otherwise, some of the north–south striking faults are not hard-linked, forming a series of relay ramps (Figure 7A).

5.2 Riedel left-lateral shear zone

The total length of this segment is approximately 18 km. Five major positive relief parts are present along the principal displacement zone (Figures 7A, 8A). The seismic cross-sections

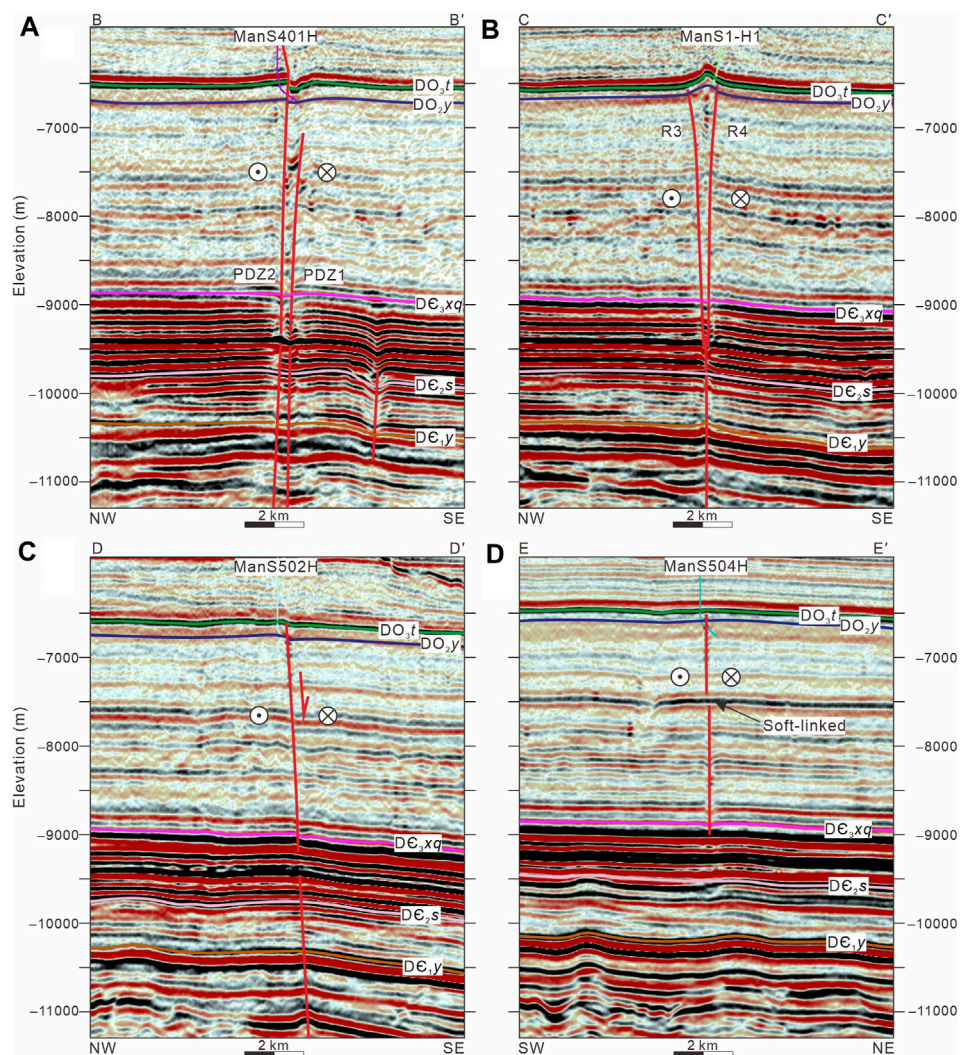


FIGURE 6

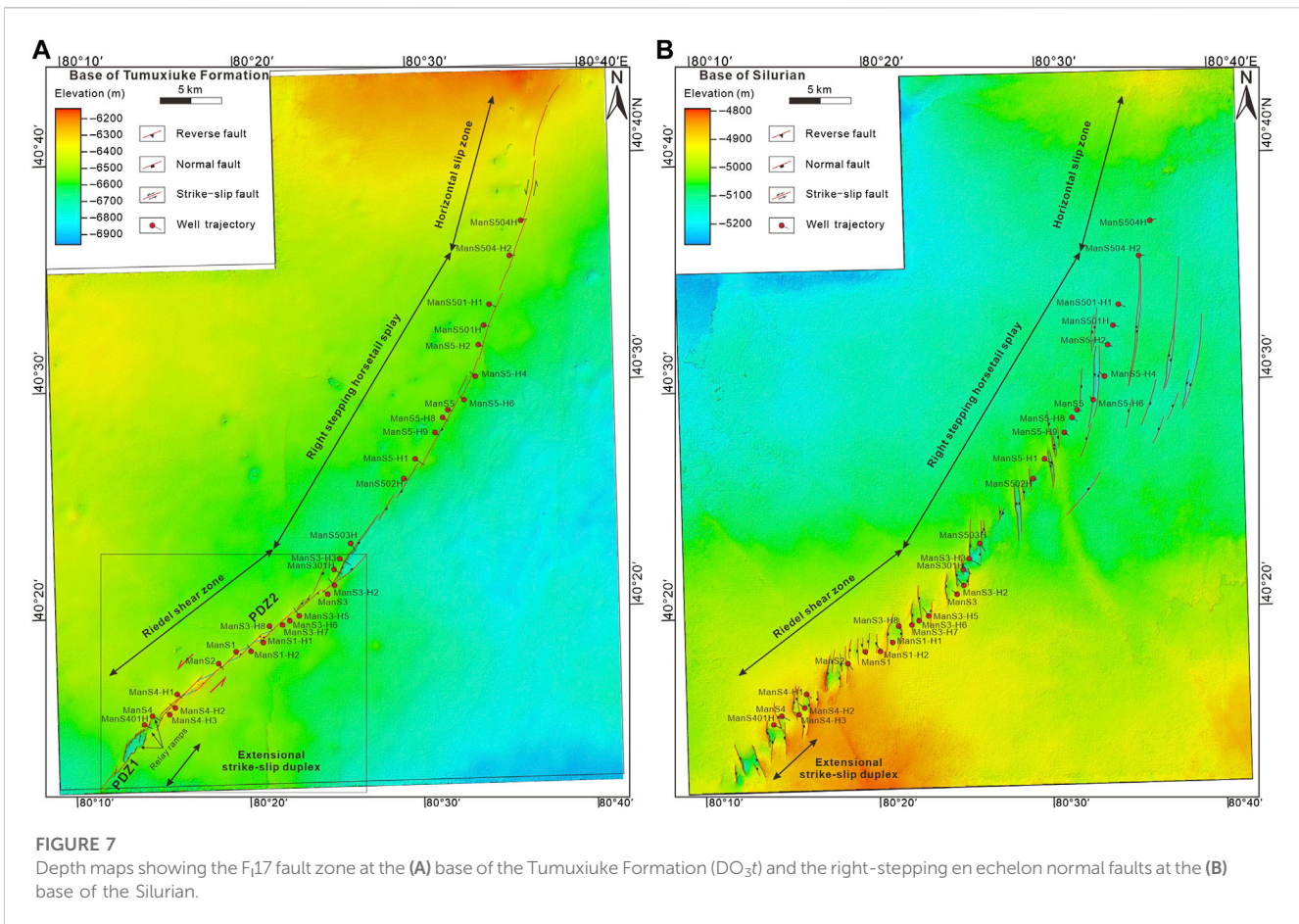
Interpreted seismic cross-sections showing the typical features of the (A) extensional strike-slip duplex, (B) pop-up structure in the Riedel shear zone, (C) extensional structure in the right-stepping horsetail splay, and (D) horizontal slip zone (see Figure 3 for locations).

show that the rocks are uplifted between the two boundary faults (Figure 6B), indicating a local compressional setting. In strike-slip deformation, local compression zones are caused by either the left-lateral slipping of right-stepping shear faults or the right-lateral slipping of left-stepping shear faults (e.g., [Sylvester, 1988](#)). As mentioned previously, the extensional strike-slip duplex indicates that the F₁₇ fault zone mainly experienced left-lateral strike-slip deformation. Therefore, only the right-stepping shear faults [synthetic (R) shears] can form a compressional region in the overlapping position. This series of shear faults mainly strikes NE47°, and their lengths are 4.5 km (R1), 5.0 km (R2), 4.0 km (R3), 3.7 km (R4), and 2.8 km (R5). Otherwise, there are another series of shear faults linking the neighboring R shears. They strike NE65°, and their lengths are 1.3 km (P1), 1.5 km (P2), 1.2 km (P3), 0.9 km (P4), 0.7 km (P5), and 0.8 km (P6) from south to north (Figure 8). In summary, this fault segment is characterized a series of elongated blocks bounded by various arrangements of R and P shears, which is a usual pattern in the Riedel simple shear model.

5.3 Right-stepping horsetail splay

In this segment, the strikes of faults change from NE45° to NE35° with a length of ~30.2 km (Figure 7A). In sectional view, a single east-dipping transtensional fault is developed in the Cambrian–Ordovician sequence (Figure 6C). Five of these kinds of faults constitute a right-stepping fault zone. These faults do not overlap with each other. In the relief–distance plots, the relief values of this segment are distinctly smaller than those of the extensional strike-slip duplex and Riedel left-lateral shear segments (<80 m), indicating a smaller deformation zone.

On the structural map of the base of the Silurian, the distribution of en echelon normal faults shows a horsetail splay pattern (Figure 7B). Correspondingly, the initial position of horsetail splays exactly overlies the eastern end of PDZ2. Therefore, this segment is a typical horsetail splay structure in which the strain distribution diverges toward the northeast.



5.4 Horizontal slip zone

At the northeast margin of the F_{17} fault zone, there is almost no relief between the two sides of the faults. The length of this segment is approximately 14.8 km and is mainly characterized by ‘string of beads’ seismic responses. The seismic cross-section shows that two independent single faults developed separately in the upper Cambrian–Middle Ordovician sequence (Figure 6D). These two faults are soft-linked at this position but hard-linked in the adjacent area, showing the lateral propagation growth and linkage process.

6 Fault-controlled reservoir distribution and connectivity

6.1 Fault zone width and reservoir width

In fault zone width–distance plots, the width is closely related to fault segmentation (Figure 8; Supplementary Table S1). Focusing on the base of the Tumuxiuke Formation (DO_{3t}), the fault zone width exhibits rapid change along strike, ranging from 362 to 2,518 m (Figure 8C). Each peak value corresponds to the overlapping or stepping position of two neighboring faults. For instance, the width of the extensional strike-slip duplex between PDZ1 and PDZ2 is up to 1,684 m (box 1 in Figure 8). The width of the pop-up structure caused by two overlapping synthetic shears (R) is up to 2,033 m (box 2 in Figure 8), while the width of the relay ramp caused by two right

stepping transtensional faults is up to 1,592 m (box 3 in Figure 8). These two plots (relief–distance and fault zone width–distance) show high positive correlations, namely, the regions with greater relief (both positive and negative) also have wider fault zones.

After validation of borehole data, we reveal that the reservoir widths in the extensional strike-slip duplex, Riedel shear zone, and right-stepping horsetail splay range from 505 m to 1,594 m (Figure 8). In the reservoir width–fault zone width plot, several types of trend lines can generally fit the relationship between them, such as linear, logarithmic, polynomial, and power law (Figure 9; Supplementary Table S2). The determination coefficient (R^2) is an indicator of the fitting degree between the estimated value of the trend line and the actual data. The value of R^2 is in the range of zero to one. The higher the value of R^2 is, the better the fitting degree. Therefore, a logarithmic function relation [$y = 740.53 \ln(x) - 3,906.6$] is the best fitting relation, which has the highest value R^2 value (0.6015). In other words, this plot reflects that the reservoir distribution is closely related to the fault zone width and that the reservoir width is positively related to the fault zone width.

6.2 Reservoir connectivity analysis

In terms of reservoir connectivity, faults are the main channels of fluid migration. The seismic cross-sections parallel to the strike of the fault show that the fault surfaces are characterized by a chaotic seismic reflection configuration, in contrast to the continuous reflection of the

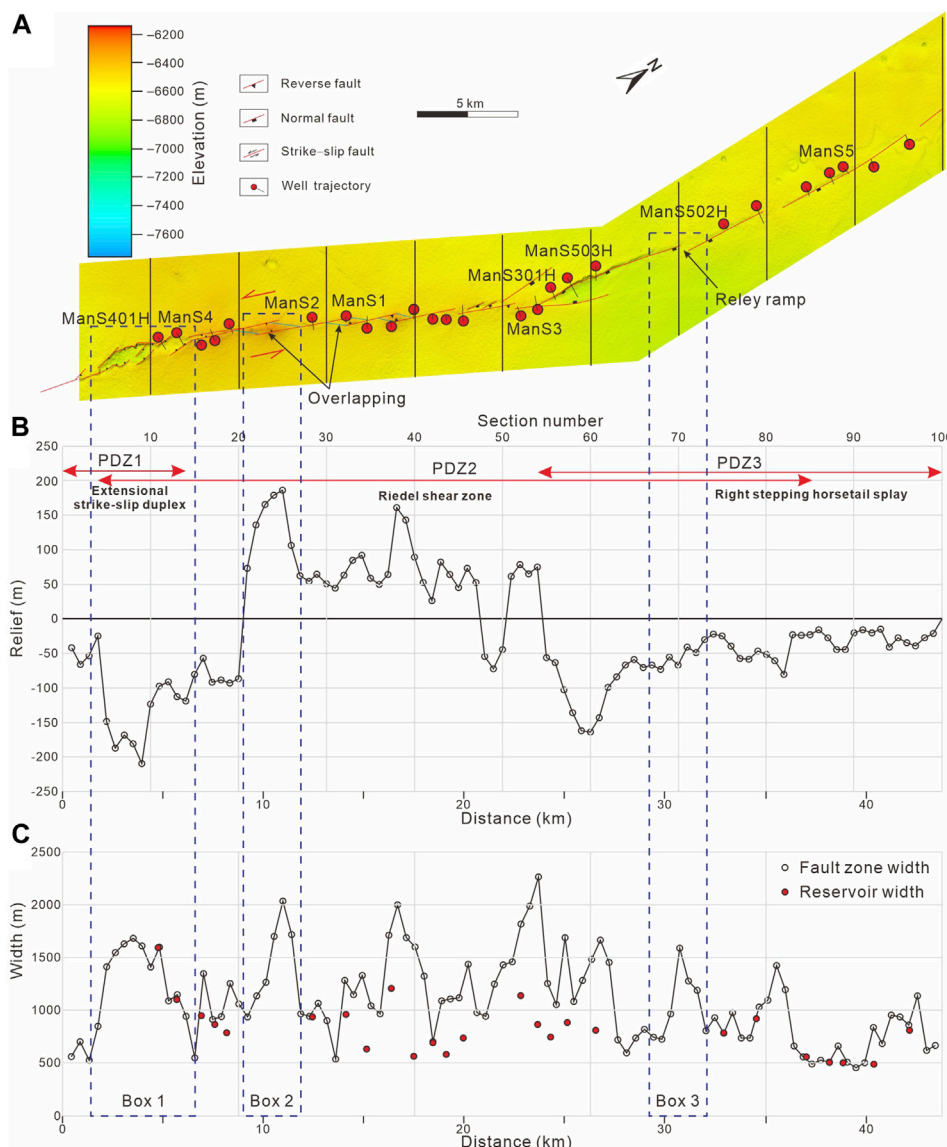


FIGURE 8 (A) Structural map (base of the Tumuxiuke Formation, DO_3^t) of the F_{17} fault zone, showing the extensional strike-slip duplex, Riedel shear zone, and right-stepping horsetail splay. (B) Structural relief–distance plot showing that the overlapping and stepping zones have greater structural relief. (C) Fault zone width–distance and reservoir width–distance plots.

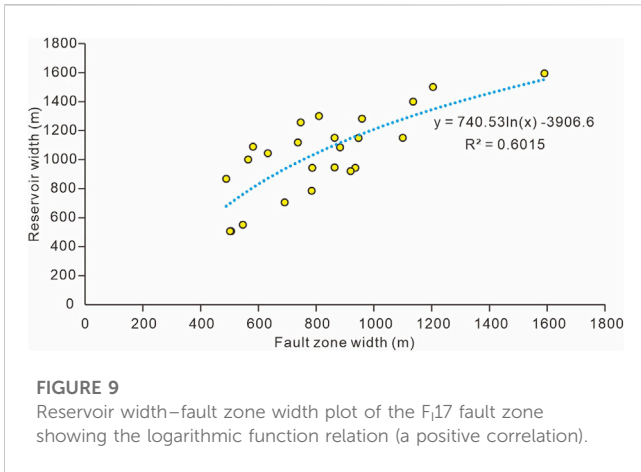
adjacent unbroken rocks (Figure 10). The established structural framework of the F_{17} fault zone indicates that the reservoirs penetrated by wells ManS4-H3, ManS4-H2, and ManS4-H1 are connected by a synthetic shear fault (R1) (Figures 10A, 11). Although the reservoir penetrated by well ManS4 is not located at R1, it is hard-linked with this synthetic shear fault. The reservoirs penetrated by wells ManS2 and ManS1 are connected by a synthetic shear fault (R2) (Figures 10B, 11). Although the reservoir penetrated by well ManS1-H2 is not linked by R2, it is located at the same pop-up structure as the wells that ManS2 and ManS1 penetrated, and this structure is characterized by a highly permeable fracture system. The reservoirs penetrated by wells ManS1-H1, ManS3-H8, ManS3-H7, and ManS3-H6 are linked by R4 (Figures 10C, 11). The reservoirs penetrated by wells ManS3 and ManS3-H2 are also linked by the same fault surface (Figures 10D, 11). This shear fault is nearly parallel to the

principal displacement zone; thus, we interpreted it as a low-angle shear (Y).

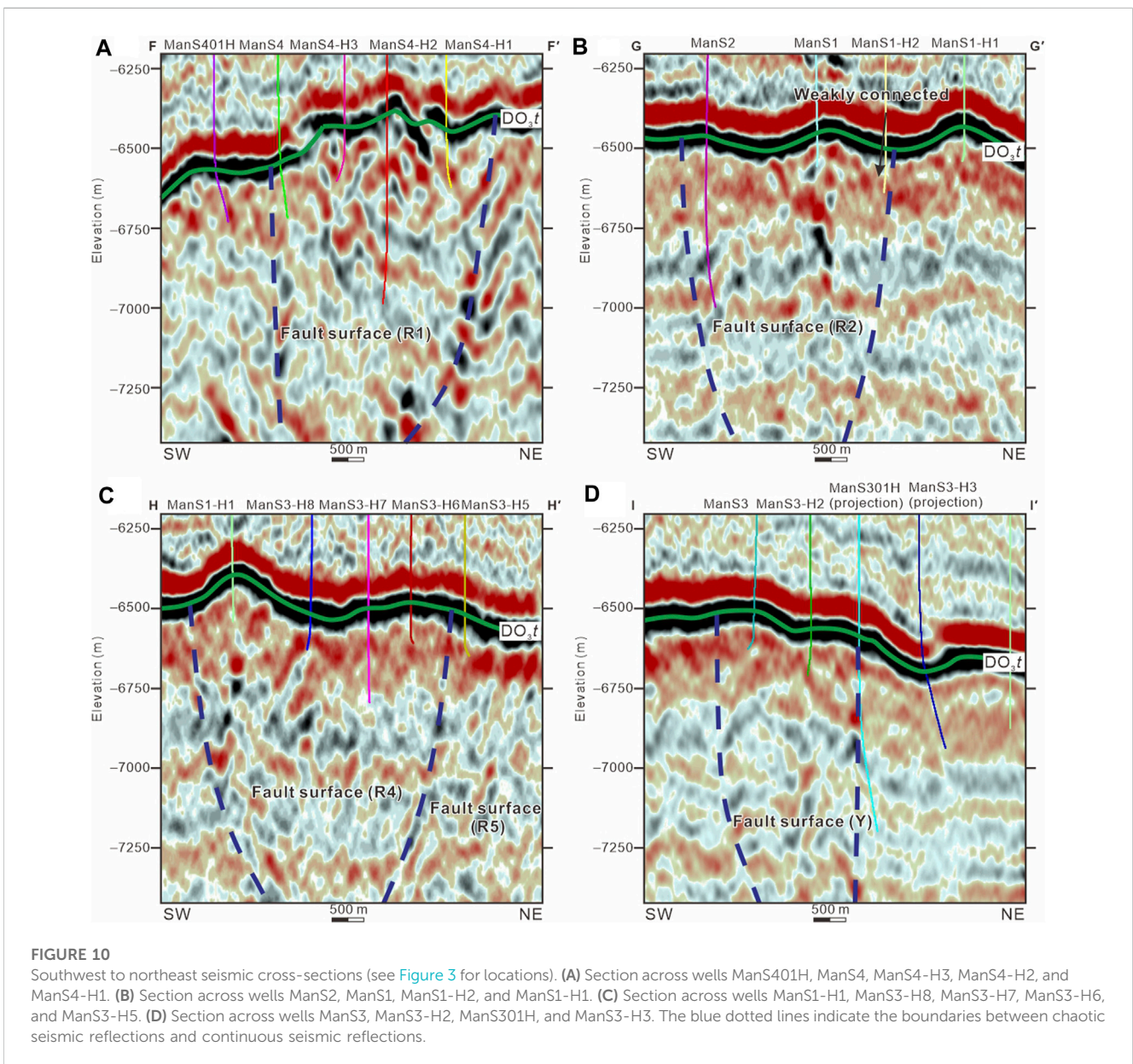
7 Discussion

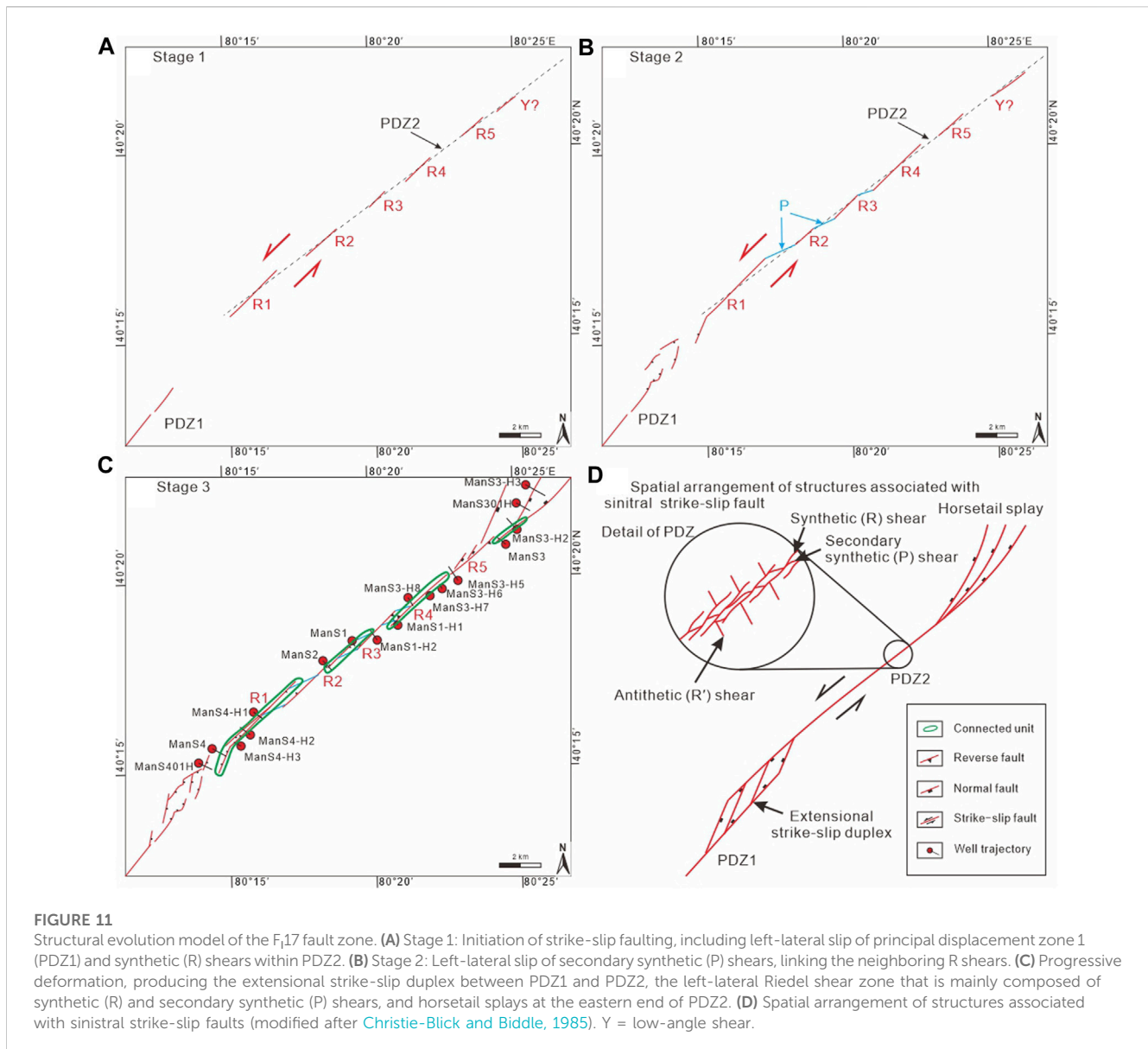
7.1 Kinematic evolution of the F_{17} fault zone

Field work (e.g., Christie-Blick and Biddle, 1985) and physical and numerical analog modeling (Dooley and Schreurs, 2012; Asaoka et al., 2016) of intraplate strike-slip tectonics suggest that a long-distance strike-slip fault is composed of secondary associated structural elements (Sylvester, 1988). Furthermore, the occurrence of these elements has a certain sequence, such as in a Riedel shear model (Tchalenko, 1970; Dooley and Schreurs, 2012). For instance, synthetic



shear (R), secondary synthetic shear (P), and low-angle shear (Y) appear successively, and antithetic (R') shear is usually rare in nature (Keller et al., 1982; Sylvester, 1988; Venâncio and da Silva, 2023). A typical pattern of a principal displacement zone is composed of R, P, and R' shears (e.g., Figure 11D). According to our interpretation, the Riedel left-lateral shear segment is mainly composed of R and P shears. Therefore, we suggest that the formation of the Riedel shear segment has three kinematic evolutionary stages: 1) the R shears initiated and laterally grew (Figure 11A); 2) the P shear initiated and linked to the neighboring R shears (Figure 11B); and 3) with the progressive growth of the R and P shear system, the present-day PDZ formed (Figure 11C). In structures associated with strike-slip faults, both releasing bends and extensional strike-slip duplexes may form rhombic grabens. Genetically, a releasing bend was formed due to progressive movement of a bent strike-slip fault (Christie-Blick and Biddle,





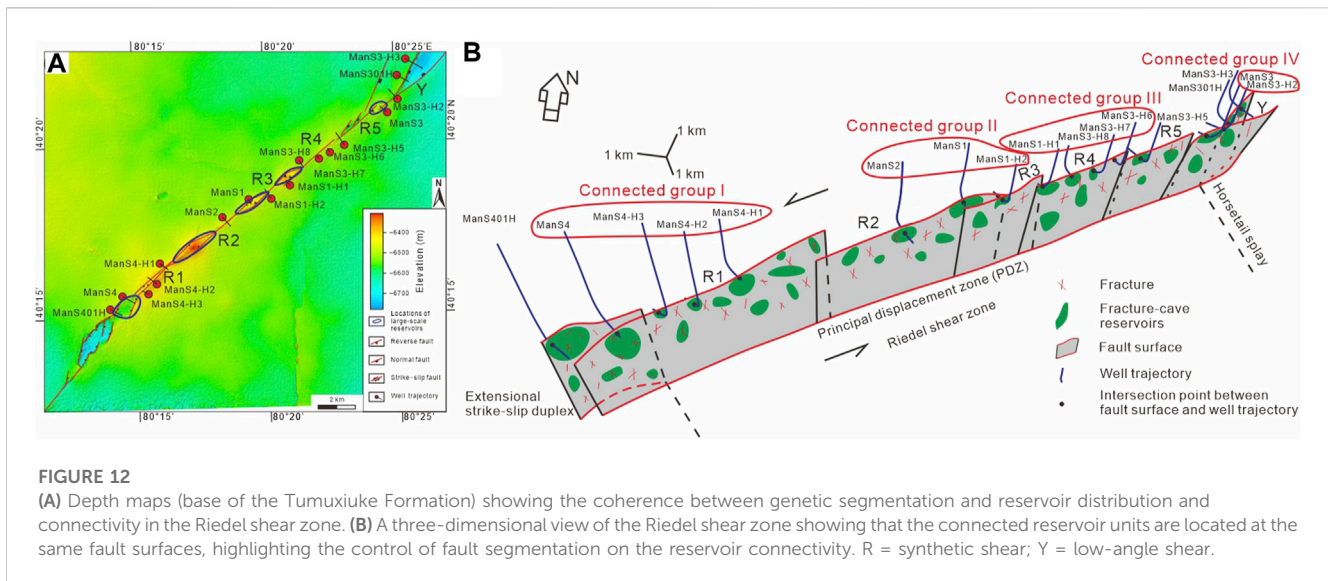
1985; Song et al., 2013). An extensional strike-slip duplex was formed due to the shearing of two stepping boundary faults. For the graben in the southwestern part of the F₁₇ fault zone, there are two independent principal displacement zones rather than a bend fault (Figures 11A, B). Each fault within the graben has a relatively small displacement (secondary linked fault). Therefore, we suggest that the extensional strike-slip duplex is a more appropriate definition. For horsetail splays, normal faults usually initiate after the formation of the PDZ. Therefore, the kinematic evolution of the horsetail splay is slightly later than the evolution of the R and P shear systems (Figure 11C).

7.2 Fault segmentation and reservoir connectivity

Since the reservoir in the Fuman oilfield has been defined as a fault-controlled fracture-cave carbonate reservoir (e.g., Huang et al., 2022), the geometry of the fault zone directly influences the reservoir

distribution. The reservoir spaces are mainly located in the fault core and damage zone within the strike-slip deformation zone (Bruhn et al., 1994; Caine et al., 1996; Berg and Skar, 2005). In the F₁₇ fault zone, the large-scale reservoirs (indicated by a wider reservoir distribution) are mainly in the overlapping or stepping zone (Figure 8). In fault zone width–reservoir width plots, a positive correlation is presented, indicating that the reservoir distribution is controlled by the lateral segmentation of the strike-slip fault (Figure 9).

In a fault zone, fractures, connected pores, and induced fractures are potential channels for fluid migration, which has been exemplified in several cases (e.g., Zeng et al., 2022; Fu et al., 2023; Gong et al., 2023). When there are two or more faults (relay or overlap, soft- or hard-linked), the increased structural complexity increases the numbers of faults and fractures and gives a wider range of orientations than for single, isolated faults (e.g., Sibson, 1996; Peacock and Parfitt, 2002; Kim et al., 2004; Fossen et al., 2005). Thus, the overlapping zones provide a wider range of



fluid flow patterns (e.g., Fossen and Rotevatn, 2016), promoting hydrocarbon migration.

During the intermittent stage of faulting, most fractures and induced fractures are sealed, causing most damage zones to have no capacity for migrating fluids. In the fault core and damage zone–fault core transition areas (Billi et al., 2003), several formation microimagers (FMIs) indicate brecciated limestones with high porosity and permeability (e.g., Deng et al., 2022). Therefore, the neighboring pores within the same fault cores are more likely connected with each other. This interpretation is consistent with the previous model, suggesting that the fluid usually migrated through the connected pores (Sun et al., 2012). According to the established evolution model of the F₁₇ fault zone, the reservoirs that connect with each other, such as the reservoir connected groups I–IV, are mainly located at the same synthetic shear fault surface (Figure 12). The connected pores are mainly located at the fault cores and damage zone–fault core transition areas, namely, around the fault slip surfaces. Therefore, different shear faults along the strike provide independent connected reservoir units. We suggest that the unique fault segmentation (lateral growth and linkage of segmented shear faults) controls the reservoir distribution and connectivity.

8 Conclusion

The genetic segmentation model that considers the lateral growth and linkage of intracratonic strike-slip faults provides a comprehensive understanding of the formation mechanism of faults, thereby helping to explain the fault-controlled reservoir distribution pattern. Combined with a high-resolution 3D seismic survey, borehole data and production dynamic data, we analyzed the relationship between fault segmentation and reservoir distribution and their connectivity and drew the following conclusion:

The structural framework of the F₁₇ fault zone in the Tarim Basin is characterized by a single fault zone in the lower–middle

Cambrian sequence, pop-up or pull-apart structures in the upper Cambrian–Middle Ordovician sequence, right-stepping en echelon normal faults in the Upper Ordovician–Permian sequence, and much smaller displacement normal fault arrays in the Triassic–Jurassic sequence. Genetically, the strike-slip fault in the Ordovician carbonate sequence consists of four segments, including an extensional strike-slip duplex, Riedel left-lateral shear zone, right-stepping horsetail splay, and horizontal slip zone from south to north. A natural logarithm correlation between reservoir width and fault zone width is revealed, indicating that the large-scale reservoirs are mainly distributed in the overlapping or stepping zones of strike-slip faults. Reservoirs, which are linked by the same lateral growth shear faults, usually show good connectivity. We suggest that segmentation (characterized by fault overlapping or stepping) and lateral linkage of intracratonic strike-slip faults control the reservoir distribution and connectivity. This study highlights the significance of recognizing the growth and lateral linkage of strike-slip faults, which may provide support for fault-controlled carbonate reservoir prediction.

Data availability statement

The original contributions presented in the study are included in the article/Supplementary Material, further inquiries can be directed to the corresponding author.

Author contributions

XD: Conceptualization, Writing–review and editing, Resources, Supervision. JC: Conceptualization, Data curation, Formal Analysis, Investigation, Methodology, Software, Writing–original draft, Writing–review and editing. PC: Conceptualization, Funding acquisition, Project administration,

Writing–review and editing. YZ: Resources, Writing–review and editing. XL: Resources, Writing–review and editing. SC: Formal Analysis, Writing–review and editing. JS: Investigation, Writing–review and editing. YD: Formal Analysis, Writing–review and editing. MW: Data curation, Writing–review and editing.

Acknowledgments

We thank the PetroChina Tarim Oilfield Company for providing the seismic and borehole data.

Conflict of interest

The authors declare that this study received funding from China National Petroleum Corporation (CNPC) Scientific Research and Technology Development Project (Grant No. 2021DJ1501). The funder had the following involvement in the study: Study design, Data collection, and Decision to publish.

Authors XD, YZ, and XL were employed by PetroChina Tarim Oilfield Company.

References

- Asaoka, A., Sawada, Y., and Yamada, S. (2016). Riedel shear band formation with flower structures that develop at the surface ground on a strike slip fault. *Jpn. Geotech. Soc. Spec. Publ.* 2, 751–754. doi:10.3208/jgssp.JPN-121
- Aydin, A., and Page, B. M. (1984). Diverse Pliocene-Quaternary tectonics in a transform environment, San Francisco Bay region, California. *Geol. Soc. Am. Bull.* 95, 1303–1317. doi:10.1130/0016-7606(1984)95<1303:DPTIAT>2.0.CO;2
- Berg, S. S., and Skar, T. (2005). Controls on damage zone asymmetry of a normal fault zone: outcrop analyses of a segment of the moab fault, SE Utah. *J. Struct. Geol.* 27, 1803–1822. doi:10.1016/j.jsg.2005.04.012
- Billi, A., Salvini, F., and Storti, F. (2003). The damage zone-fault core transition in carbonate rocks: implications for fault growth, structure and permeability. *J. Struct. Geol.* 25, 1779–1794. doi:10.1016/S0191-8141(03)00037-3
- Bruhn, R. L., Parry, W. T., Yonkee, W. A., and Thompson, T. (1994). Fracturing and hydrothermal alteration in normal fault zones. *pure Appl. Geophys.* 142, 609–644. doi:10.1007/BF00876057
- Caine, J. S., Evans, J. P., and Forster, C. B. (1996). Fault zone architecture and permeability structure. *Geology* 24, 1025–1028. doi:10.1130/0091-7613(1996)024<1025:FZAAPS>2.3.CO;2
- Cartwright, J. A., Mansfield, C., and Trudgill, B. (1996). The growth of normal faults by segment linkage. *Geol. Soc. Spec. Publ.* 99, 163–177. doi:10.1144/GSL.SP.1996.099.01.13
- Chen, C., Lu, H., Jia, D., Cai, D., and Wu, S. (1999). Closing history of the southern tianshan oceanic basin, western China: an oblique collisional orogeny. *Tectonophysics* 302, 23–40. doi:10.1016/S0040-1951(98)00273-X
- Chen, J., He, D., Tian, F., Huang, C., Ma, D., and Zhang, W. (2022). Control of mechanical stratigraphy on the stratified style of strike-slip faults in the central Tarim Craton, NW China. *Tectonophysics* 830, 229307. doi:10.1016/j.tecto.2022.229307
- Christie-Blick, N., and Biddle, K. T. (1985). Deformation and basin formation along strike-slip faults. *Strike-Slip Deform. Basin Form. Sediment.* 37, 1–34. doi:10.2110/pec.85.37.0001
- Clayton, L. (1966). Tectonic depressions along the hope fault, a transcurrent fault in North Canterbury, New Zealand. *New zeal. J. Geol. geophys.* 9, 95–104. doi:10.1080/00288306.1966.10420198
- Deng, S., Li, H., Zhang, Z., Wu, X., and Zhang, J. (2018). Characteristics of differential activities in major strike-slip fault zones and their control on hydrocarbon enrichment in Shunbei area and its surroundings, Tarim Basin. *Oil Gas. Geol.* 39, 878–888. doi:10.11743/ogg20180503
- Deng, S., Li, H., Zhang, Z., Zhang, J., and Yang, X. (2019). Structural characterization of intracratonic strike-slip faults in the central Tarim Basin. *Am. Assoc. Pet. Geol. Bull.* 103, 109–137. doi:10.1306/06071817354
- The remaining authors declare that the research was conducted in the absence of any commercial or financial relationships that could be construed as a potential conflict of interest.

Publisher's note

All claims expressed in this article are solely those of the authors and do not necessarily represent those of their affiliated organizations, or those of the publisher, the editors and the reviewers. Any product that may be evaluated in this article, or claim that may be made by its manufacturer, is not guaranteed or endorsed by the publisher.

Supplementary material

The Supplementary Material for this article can be found online at: <https://www.frontiersin.org/articles/10.3389/feart.2023.1255162/full#supplementary-material>

SUPPLEMENTARY TABLE S1

Measured structural reliefs and fault zone widths from 99 cross-sections.

SUPPLEMENTARY TABLE S2

Measured fault zone widths and reservoir widths from 24 wells.

- Huang, C., Yun, L., Cao, Z., Lv, H., Li, H., Liu, Y., et al. (2022). Division and formation mechanism of fault-controlled fracture-vug system of the Middle-to-Lower Ordovician, Shunbei area, Tarim Basin. *Oil Gas. Geol.* 43, 54–68. doi:10.11743/ogg20220105
- Jia, C. (1997). *Tectonic characteristics and petroleum, Tarim Basin*. China, Beijing: Petroleum Industry Press.
- Keller, E. A., Bonkowski, M. S., Korsch, R. J., and Shlemon, R. J. (1982). Tectonic geomorphology of the san andreas fault zone in the southern indio hills, coachella valley, California. *GSA Bull.* 93, 46–56. doi:10.1130/0016-7606(1982)93<46:TGOTSA>2.0.CO;2
- Kim, Y. S., Peacock, D. C. P., and Sanderson, D. J. (2004). Fault damage zones. *J. Struct. Geol.* 26, 503–517. doi:10.1016/j.jsg.2003.08.002
- Li, F., Wei, J., Di, B., Pan, W., Zheng, D., Wan, X., et al. (2012). Formation mechanism research for bead-like seismic reflection of carbonate caves. *Oil Geophys. Prospect* 47, 385–391.
- Liu, B., Qi, L., Li, Z., Liu, J., Huang, C., Yang, L., et al. (2020). Spatial characterization and quantitative description technology for ultra-deep fault-karst reservoirs in the Shunbei area. *Acta Pet. Sin.* 41, 412–420. doi:10.7623/syxb202004004
- Liu, Y., Suppe, J., Cao, Y., Hao, F., Liu, Y., Wang, X., et al. (2023). Linkage and formation of strike-slip faults in deep basins and the implications for petroleum accumulation: A case study from the shunbei area of the Tarim Basin, China. *Am. Assoc. Pet. Geol. Bull.* 107, 331–355. doi:10.1306/11142220110
- Ma, D., Wu, G., Zhu, Y., Tao, X., Chen, L., Li, P., et al. (2019). Segmentation characteristics of deep strike slip faults in the Tarim Basin and its control on hydrocarbon enrichment: taking the ordovician strike slip fault in the halahatang oilfield in the tabei area as an example. *Earth Sci. Front.* 26, 225–237. doi:10.13745/j.esf.sf.2019.1.10
- Mann, P. (2007). Global catalogue, classification and tectonic origins of restraining- and releasing bends on active and ancient strike-slip fault systems. *Geol. Soc. Lond. Spec. Publ.* 290, 13–142. doi:10.1144/SP290.2
- Matte, P., Tapponnier, P., Arnaud, N., Bourjot, L., Avouac, J. P., Vidal, P., et al. (1996). Tectonics of western tibet, between the Tarim and the indus. *Earth Planet. Sci. Lett.* 142, 311–330. doi:10.1016/0012-821x(96)00086-6
- Ning, F., Jin, Z., Zhang, Z., Yun, J., and Zhang, J. (2018). Mechanism of strike-slip faulting and hydrocarbon accumulation in northern slope of Tazhong area. *Oil Gas. Geol.* 39, 98–106. doi:10.11743/ogg20180110
- Pakiser, L. C. (1960). Transcurrent faulting and volcanism in owens valley, California. *Bull. Geol. Soc. Am.* 71, 153–160. doi:10.1130/0016-7606(1960)71[153:TFAVIO]2.0.CO;2
- Peacock, D. C. P., and Parfitt, E. A. (2002). Active relay ramps and normal fault propagation on Kilauea Volcano, Hawaii. *J. Struct. Geol.* 24, 729–742. doi:10.1016/S0191-8141(01)00109-2
- Qi, L. (2020). Characteristics and inspiration of ultra-deep fault-karst reservoir in the Shunbei area of the Tarim Basin. *China Pet. explor.* 25, 102–111. doi:10.3969/j.issn.1672-7703.2020.01.010
- Qiao, Z., Shen, A., Zhang, S., Hu, A., Liang, F., Luo, X., et al. (2023). Origin of giant Ordovician cavern reservoirs in the Halahatang oil field in the Tarim Basin, northwestern China. *Am. Assoc. Pet. Geol. Bull.* 107, 1105–1135. doi:10.1306/11152219193
- Shi, K., Liu, B., Jiang, W., Luo, Q., and Gao, X. (2018). Nanhua-sinian tectono-sedimentary framework of Tarim Basin, NW China. *Oil Gas. Geol.* 39, 862–877. doi:10.11743/ogg20180502
- Sibson, R. H. (1996). Structural permeability of fluid-driven fault-fracture meshes. *J. Struct. Geol.* 18, 1031–1042. doi:10.1016/0191-8141(96)00032-6
- Sobel, E. R., and Dumitru, T. A. (1997). Thrusting and exhumation around the margins of the western Tarim basin during the India-Asia collision. *J. Geophys. Res. Solid Earth* 102, 5043–5063. doi:10.1029/96JB03267
- Song, H., Zhang, C., and Wang, G. (2013). *Structural geology*. Beijing: Geological Publishing House.
- Sun, Q., Fan, T., Gao, Z., Wu, J., Zhang, H., Jiang, Q., et al. (2021). New insights on the geometry and kinematics of the Shunbei 5 strike-slip fault in the central Tarim Basin, China. *J. Struct. Geol.* 150, 104400. doi:10.1016/j.jsg.2021.104400
- Sun, T., Fu, G., Lv, Y., and Zhao, R. (2012). A discussion on fault conduit fluid mechanism and fault conduit form. *Geol. Rev.* 58, 1081–1090. doi:10.3969/j.issn.0371-5736.2012.06.008
- Sylvester, A. G. (1988). Strike-slip faults. *Bull. Geol. Soc. Am.* 100, 1666–1703. doi:10.1130/0016-7606(1988)100<1666:SSF>2.3.CO;2
- Tchalenko, J. S. (1970). Similarities between shear zones of different magnitudes. *GSA Bull.* 81, 1625–1640. doi:10.1130/0016-7606(1970)81[1625:SBSZOD]2.0.CO;2
- Tian, J., Yang, H., Zhu, Y., Deng, X., Xie, Z., Zhang, Y., et al. (2021). Geological conditions for hydrocarbon accumulation and key technologies for exploration and development in Fuman oilfield, Tarim Basin. *Acta Pet. Sin.* 42, 971–985. doi:10.7623/syxb202108001
- Venâncio, M. B., and da Silva, F. C. A. (2023). Structures evolution along strike-slip fault zones: the role of rheology revealed by PIV analysis of analog modeling. *Tectonophysics* 851, 229764. doi:10.1016/j.tecto.2023.229764
- Walsh, J. J., Bailey, W. R., Childs, C., Nicol, A., and Bonson, C. G. (2003). Formation of segmented normal faults: A 3-D perspective. *J. Struct. Geol.* 25, 1251–1262. doi:10.1016/S0191-8141(02)00161-X
- Walsh, J. J., and Watterson, J. (1988). Analysis of the relationship between displacements and dimensions of faults. *J. Struct. Geol.* 10, 239–247. doi:10.1016/0191-8141(88)90057-0
- Wang, L., Deng, S., Zhang, Z., Zhang, J., and Wen, S. (2017). Development characteristics and petroleum geological significance of string beads in 3D seismic region of northern Shun 8 block. *Spec. Oil Gas. Reserv.* 2017, 66–71. doi:10.3969/j.issn.1006-6535.2017.06.013
- Whipp, P. S., Jackson, C. A. L., Schlische, R. W., Withjack, M. O., and Gawthorpe, R. L. (2017). Spatial distribution and evolution of fault-segment boundary types in rift systems: observations from experimental clay models. *Geol. Soc. Spec. Publ.* 439, 79–107. doi:10.1144/SP439.7
- Woodcock, N. H., and Fischer, M. (1986). Strike-slip duplexes. *J. Struct. Geol.* 8, 725–735. doi:10.1016/0191-8141(86)90021-0
- Xu, Z., Yang, J., Li, H., Zhang, J., Zeng, L., and Jiang, M. (2006). The qinghai-tibet plateau and continental dynamics: A review on terrain tectonics, collisional orogenesis, and processes and mechanisms for the rise of the plateau. *Geol. China* 33, 221–238. doi:10.3969/j.issn.1000-3657.2006.02.001
- Yang, P., Wu, G., Nuriel, P., Nguyen, A. D., Chen, Y., Yang, S., et al. (2021). *In situ* LA-ICPMS U Pb dating and geochemical characterization of fault-zone calcite in the central Tarim Basin, northwest China: implications for fluid circulation and fault reactivation. *Chem. Geol.* 568, 120125. doi:10.1016/j.chemgeo.2021.120125
- Yang, X., Xu, X., Qian, Y., Chen, Q., Chu, C., and Jiang, H. (2014). Discussion on regional differences of basement composition of the Tarim Basin, NW China. *Geotecton. Metallog.* 38, 544–556.
- Yuan, X. (1996). *Geophysical atlas of China*. Beijing: Geological Publishing House.
- Yun, L. (2021). Controlling effect of NE strike-slip fault system on reservoir development and hydrocarbon accumulation in the eastern Shunbei area and its geological significance, Tarim Basin. *China Pet. explor.* 26, 41–52. doi:10.3969/j.issn.1672-7703.2021.03.004
- Zeng, L., Gong, L., Guan, C., Zhang, B., Wang, Q., Zeng, Q., et al. (2022). Natural fractures and their contribution to tight gas conglomerate reservoirs: A case study in the northwestern sichuan basin, China. *J. Pet. Sci. Eng.* 210, 110028. doi:10.1016/j.petrol.2021.110028
- Zhang, J., Zhang, Z., Xu, Z., Cui, J., and Yang, J. (1999). Discovery of khondalite series from the western segment of Altyn and their petrological and geochronological studies. *Sci. China (Series D)* 29, 298–305. doi:10.3969/j.issn.1674-7240.1999.04.002
- Zhao, P., He, J., Deng, C., Chen, Y., and Mitchell, R. N. (2021). Early Neoproterozoic (870–820 Ma) amalgamation of the Tarim craton (northwestern China) and the final assembly of Rodinia. *Geology* 49, 1277–1282. doi:10.1130/G48837.1
- Zhou, B., Chen, H., Yun, L., and Tang, D. (2022). The relationship between fault displacement and damage zone width of the paleozoic strike-slip faults in shunbei area, Tarim Basin. *Earth Sci.* 47, 437–451. doi:10.3799/dqkx.2021.073